Chin. J. Astron. Astrophys. Vol. 7 (2007), No. 6, 789–802
(*http://www.chjaa.org*)

Chinese Journal of
Astronomy and
Astrophysics

Radio Phase-Resolved Spectra of the Conal-Double Pulsar B1133+16 *

Jian-Ling Chen[1], Hong-Guang Wang[1], Wan-Hai Chen[1], Hui Zhang[2] and Yi Liu[1]

[1] Center for Astrophysics, Guangzhou University, Guangzhou 510006; *chenjianling62@163.com*
[2] National Astronomical Observatories, Chinese Academy of Sciences, Beijing 100012

Received 2007 March 13; accepted 2007 April 21

Abstract Based on dividing the profile into a number of absolute phase intervals, the phase-resolved spectra (PHRS) are derived from published time-aligned average profiles at radio frequencies over two decades for the classic conal-double pulsar B1133+16. The relative spectral index, defined as the difference between the spectral indices of a reference and the given arbitrary phase interval, is obtained by power-law fit at each phase interval. The derived phase-resolved spectra show an "M-like" shape, of which the leading part and trailing part are approximately symmetrical. The basic feature of the PHRS is that the spectrum first flattens then steepens as the pulse phase sweeps from the profile center to the profile edges. The PHRS provide a coherent explanation of the major features of profile evolution of B1133+16, namely, the pulse width shrinkage with increasing frequency and the frequency evolution of the relative intensity between the leading and trailing conal components, and the bridge emission. The PHRS may be an indicator for emission spectral variation across the pulsar magnetosphere. Possible mapping from PHRS to emission-location-dependent spectral variation is presented, and some intrinsic mechanisms are discussed.

Key words: pulsars: individual (B1133+16) — method: data analysis

1 INTRODUCTION

Most pulsars have profiles that change with frequency. A widely considered interpretation is that the spectrum varies in the different parts (or components) of the profile. The empirical model of pulse morphological taxonomy suggests that the spectrum is generally flatter for the conal component than the core component (Rankin 1983). This suggestion was supported by later studies, e.g. Lyne & Manchester (1998, hereafter LM88) and Kramer et al. (1994, hereafter KWJ94), where the authors severally derived the spectral indices of different components for a number of pulsars. LM88 employed a method based on normalized beam radius. The angular beam radii, converted from pulse longitudes with the geometrical relations, are normalized with respect to the corresponding maximum angular radius at each frequency. Dividing each whole beam radius into a number of bins, the spectral index relative to the mean value of the outmost components is then calculated for each bin. By averaging the normalized-radius spectra of 23 pulsars with both core and conal components, LM88 found that the spectral difference between the core and conal components was consistent with Rankin's suggestion. In KWJ94, the normalized beam radius is also used but in a different way. They used Gaussian fits, which is proposed and developed by several authors (Wu et al. 1992, Wang et al. 2003, Zhang et al. 2007) to decompose the core component and conal pairs from the average pulse profiles. The relative spectral index is then figured out for each component with respect to the outmost one. Different from LM88, the KWJ94 authors used the normalized radii derived from the component-peak longitudes to denote the components. The combined results for seven pulsars confirm the tendency reported

∗ Supported by the National Natural Science Foundation of China.

by Rankin, but they also revealed a large scattering of the relative spectral indices of conal components. In fact, the spectral difference was found not only between the core and conal components, but also between different conal components (KWJ94; Wang et al. 2001; Kramer et al. 2003). This indicates that spectral fluctuation along pulse longitude is a basic feature of pulsar emission.

Unlike the method of deriving spectral index along the normalized beam radius at radio band, at high energy band the phase-dependent spectrum has been analyzed in an alternative way, the so-called phase-resolved spectrum (hereafter PHRS). In this method, absolute pulse longitude bins rather than normalized radius bins are used. For instance, the gamma-ray pulse profiles of the Crab pulsar are divided into seven phase intervals and spectral indices are determined for each (Fierro et al. 1998). Pulsars with PHRS at gamma-ray band available include the three brightest gamma-ray pulsars: Crab, Geminga and Vela (Kanbach et al. 1994; Fierro et al. 1998; Kuiper et al. 2001; Jackson & Halpern 2005). The PHRS at X-ray band is also investigated for the Crab pulsar (Mineo et al. 2006). To distinguish these two ways of deriving the spectral indices, the phase-dependent spectrum based on absolute phase intervals is called PHRS, while that based on normalized radius (equivalent to normalized pulse phase) intervals is called normalized-radius-resolved spectrum (hereafter NRRS).

Compared to the pulse arrival time at high energy band, the pulse arrival time at radio frequency suffers from additional dispersion delay relative to the infinite frequency caused by interstellar plasma dispersion measure. It is not so easy to align perfectly the profiles at different radio frequencies because of uncertainties in the DM and some other related problems, e.g. superdispersion at low frequencies (Phillips 1991). Therefore, NRRS is an easier way to study the phase-dependent spectra. However, considering that the same normalized-radius bin corresponds to different absolute phase intervals at various frequencies and that different absolute phases are related to different magnetospheric emission regions, what one actually derives is a spectral index from intensities in different regions, where the physical and geometrical parameters, and even the bunches of emitting particles, are not the same. The spectral index derived with NRRS does not exactly reflect the emission properties for a particular location in the pulsar magnetosphere. Therefore, the PHRS based on absolute phase intervals is more physically meaningful than the NRRS. Accordingly, we will use PHRS to study the phase-dependent spectra of B1133+16 in this paper.

PSR B1133+16 is a classic and a most widely studied double-profile pulsar. Its average profile has two well separated components and is classified as the conal-double type (Rankin 1990). The frequency dependence of the pulse profile shows three basic properties: (1) The component separation or pulse width decreases continuously with frequency, and can be fitted by an expression $\Delta\theta = A\nu^{-\mu} + \Delta\theta_0$ (Thorsett 1991; Mitra & Rankin 2002), (2) The intensity of the leading component becomes stronger with respect to that of the trailing one with increasing frequency, and (3) The relative intensity of the central or bridge part of the profile with respect to the peaks decreases with frequency.

The reasons for choosing this pulsar are: First, there are essential discrepancies between the interpretations for the first and the two following phenomena. The shrinking of the pulse width is conventionally interpreted as due to radius-to-frequency mapping (RFM, Cordes 1978; Wu et al. 2002), a narrow-band model, which assumes that the higher frequency emission arises from a lower height while the lower frequency emission from a greater height. However, the spectral difference used to explain the next two phenomena is a wide-band interpretation. It is worth trying to understand these phenomena in a single frame of wide-band emission spectrum. The PHRS should be helpful in this attempt. Secondly, B1133+16 is currently the only pulsar with high quality and rich time-aligned pulse profiles studied by different groups. With the aid of simultaneous observations and mature techniques in the correction of dispersion delay and timing model, the time-aligned multi-frequency pulse profile is now available for more than 60 pulsars in the literature (e.g. Hankins & Rickett 1986; Hankins et al. 1991, hereafter HIM91; Kramer et al. 1997, hereafter KXJ97; Kuzmin et al. 1998, hereafter KIS98). Among these, B1133+16 is unique in having a very small DM and a high signal to noise ratio, and with profiles covering the widest frequency range (from 25 MHz to 10.5 GHz). The time-aligned profiles are available from at least three study groups (HIM91; KXJ97; KIS98). Therefore, reliable PHRS could be obtained by cross-checking.

This paper is organized as follows. The data source and reduction are described in Section 2. The results and their implications on the frequency evolution of the pulse profile are presented in Section 3. The derived PHRS as an indicator to spectral variation in the magnetosphere are discussed in Section 4. Our conclusions and a discussion are given in Section 5.

2 DATA REDUCTION

2.1 Description for Data Sets and Profile-selection Criteria

The multi-frequency observations are usually made at different epochs, therefore, corrections to various delay in pulse arrival times between the different frequencies are required. These include the instrumental time delay, the dispersion delay between different frequencies and the time delay between different epochs due to the pulsar period changing. The time-aligned profiles of B1133+16 are adopted from HIM91, KXJ97 and KIS98.

1. HIM91. The profiles at frequencies from 25 MHz to 4880 MHz were observed with the Arecibo 305 m telescope, the Pushchino DKR 1000 telescope and BSA array in sessions from 1988 to 1990. Observations with DKR 1000 telescope at 60, 40 and 30 MHz were simultaneously accompanied by 102.5 MHz measurements with BSA array. All the data were reduced to the barycentric arrival time. The profiles were aligned with an adjusted value $\mathrm{DM} = 4.8470\,\mathrm{pc\ cm^{-3}}$.
2. KXJ97. Observations were performed at five frequencies from 1.4 GHz to 32 GHz with the 100 m radio telescope of the MPIfR. The observation epoch is July 1994 for frequency above 2.25 GHz, and is various for 1410–1710 MHz. Except for the observations at 2.25 GHz and 8.5 GHz, the measurements were not made simultaneously at different frequencies. The Jodrell Bank timing model was employed to keep track of the pulse phase between the observations. The barycentric arrival times were converted to the arrival times at infinite radio frequency by using the DM values from the Jodrell Banks observations. Because the effect on the correction of arrival times due to DM is not so strong at high frequencies as at low frequencies, DM is not adjusted in the minimization procedure of times-of-arrival (TOA). The upper limit for a time delay between all frequencies are determined as 1.64 ms.
3. KIS98. The authors achieved alignment of 56 pulsars by means of correction of dispersion delay and reduction of the barycentric arrival times to a common frequency at a common epoch. Their data were selected from the two observations made between Aug.–Oct., 1984 and August and September in 1991, with the Large Phased Array (LPA) Radio Telescope at 102 MHz, the 76-m Lowell telescope at frequency from 230 to 1380 MHz, and the 100-m radio telescope of the MPIfR at frequency 1400 to 10500 MHz.

In order to compensate for the time delay between observations at different epochs caused by period variation, the timing model accurate to the first period derivative is used, with additional correction to the modelled period values via control measurements made at different date at the same observatory and same frequency. The catalogued DM value in Taylor et al. (1993), $\mathrm{DM} = 4.847\,\mathrm{cm^{-3}}$ pc, was used to align all profiles between 0.1 and 10 GHz. Owing to the difficulty in aligning observations stretched over long time intervals, they noted the fact that both the 1984 and 1991 measurements contained observations close to 1400 MHz and aligned the profiles measured at this frequency by the strongest components observed.

There is a slight difference in the quality of profile alignment in these data sets. This could be seen from the alignment of profile centers, determined by the middle point between the leading and trailing peaks. For HIM91, the profile centers at all frequencies are well aligned, with offsets no greater than 0.2 °. For KXJ97, the profile centers at 2.25, 4.75 and 8.5 GHz trail behind those at 1.4 and 10.5 GHz by about 0.6 °. For KIS98, the profile center at 100 MHz deviates from the others by nearly 1 °. The influence of misalignment of the profile centers is visible in the PHRS results presented in Section 3.

The DM is a crucial parameter in the profile alignment. A common stage in the alignment is to translate the arrival times at finite frequencies to that at infinite frequency (or a common frequency, as in KIS98) with the following equation (KIS98)

$$\Delta t_{\mathrm{DM}} = 10^7 (1/f_1^2 - 1/f_2^2) \times \mathrm{DM}/2.41, \tag{1}$$

where Δt_{DM}, f and DM are in units of ms, MHz and pc cm^{-3}, respectively. Owing to the f^{-2} law of dispersion delay, low-frequency profiles suffer from larger alignment uncertainty than high frequency profiles for a given discrepancy of the assumed DM value from the true value. For example, the method of microstructure cross-correlation between pairs of frequencies is considered as a better way to determine the DM than profile alignment. With this method, the measured DM values varied from $4.8462 \pm 0.0004\,\mathrm{pc\ cm^{-3}}$ (HIM91)

Table 1 Observation Log for Quoted Profiles from Three Data Sets

Paper	Quoted freq. (GHz)	Facility	Obs. epoch
HIM91	0.102, 0.111, 0.43, 1.408, 2.37, 4.87	Arecibo, BSA array	1988–1990
KXJ97	1.4, 2.25, 4.75, 8.5, 10.55	Effelsberg	1994
KIS98	0.1, 0.2, 0.4, 0.6, 1.4, 4.7	LPA, Lowell, Effelsberg	1984, 1991

to 4.8413 ± 0.0001 pc cm^{-3} (Popov et al. 1987). If the true DM value is much smaller than the value 4.8470 used by HIM91 and KIS98 in their profile alignment, e.g. $\mathrm{DM} = 4.8413$ pc cm^{-3} as obtained by Popov et al. or $\mathrm{DM} = 4.84$ pc cm^{-3} as obtained by Wang et al. (2001), then the difference of 0.0057 pc cm^{-3} causes an excess phase delay about 11° at 25 MHz, but the delay reduces to 2.3° at 100 MHz. Therefore, using aligned profiles at high frequencies, e.g. above 100 MHz, is sufficiently safe.

The profiles are selected with two criteria: above 100 MHz and high signal to noise ratio. Apart from the smaller error in the time-alignment, another reason to select profiles above 100 MHz is that the phase-averaged spectrum is a simple power-law above 100 MHz, while it turns over below 100 MHz (Kramer et al. 2003). Considering these, we discarded profiles below 100 MHz in HIM91. The profile at 10.5 GHz in KIS98 was not used either because of poor signal to noise ratio. All the other profiles were adopted. The basic information for the observations at the quoted frequencies from three data sets are summarized in Table 1.

2.2 Method of Data Reduction

In the literature only the relative intensity of pulse profiles is given. Therefore, we have to consider the relative spectral index, which does not rely on absolute pulse intensities. Noting that the phase-averaged spectrum of B1133+16 is well fitted with a single power-law over a very wide frequency range from 0.4 to 32 GHz (Maron et al. 2000), it is assumed that the spectrum at any phase interval can also be described by a single power law, i.e. $I = Kf^{-\alpha}$. The relative spectral index between a reference and a given interval is defined as $\lambda_i = \alpha_0 - \alpha_i$, and the corresponding intensity ratio is $\eta_i \equiv I_i/I_0 = K_i/K_0 f^{\lambda_i}$, where I and f are the intensity and observing frequency, the coefficient K is a constant for each phase interval, the subscripts "i" and "0" denoting the arbitrary and reference intervals, respectively. Then one has

$$\log \eta_i = \lambda_i \log f + C_i, \tag{2}$$

where $C_i = \log(K_i/K_0)$. Therefore, the relative spectral index can be obtained by least square fit to the data of η_i and f for each phase interval.

We derive the PHRS in three stages. First, the pulse profiles were taken from the electronic versions of the papers and converted into digital profiles. Secondly, the pulse profile was divided into a number of phase bins of equal width. The interval widths in the results presented were set at 0.56°, 0.49° and 0.40° for the profiles in HIM91, KIS98 and KXJ97, respectively. This ensures that the re-sampled phase interval is wider than the observational profile resolution (dominated by the smearing of observational sampling, about 0.3°) at each frequency, at the same time, it ensures that details of the PHRS are resolved. The relative intensity η_i is measured for each phase bin with respect to the reference phase bin. The latter is the phase bin that contains the leading peak at 400 MHz for both the HIM91 and KIS98 data sets and at 2250 MHz for the KXJ97 data set. The intensities in the bins are all adequate: it was found that changing the reference phase bin and re-defining the bins width did not affect the results in any essential way. See the discussion in Section 5. The baseline of off-pulse noise was given in HIM91 and KXJ97, for each frequency, but not in KIS98. In the latter case the baseline were determined by the mean values of the measured noise intensities. Finally, λ_i is obtained with least-square fit and plotted versus the central longitude of each phase bin.

The profile boundary is determined at each frequency by the 3σ level, with σ the standard deviation of the measured noise. Because the profile gets narrower with increasing frequency, the number of relative intensities that are used in the power-law fit decreases as the pulse longitude approaches the outmost leading and trailing wings of the profile at the lowest frequency. The total phase window of PHRS is determined by the boundaries where relative intensities at just three frequencies are available. The number of data points used in fit is marked with various symbols in the PHRS plots. The error of measured relative intensity

Table 2 Phase intervals and spectral-index fluctuation amplitudes in the four segments of the PHRS obtained in three data sets. See text for the segment abbreviations and the definition of $\Delta\lambda$.

Parameter	Data sets	Leading − LO	segments LI	Trailing − TI	segments TO
Interval (deg.)	HIM91	4.2	2.8	2.3	4.7
	KIS98	4.6	2.4	2.0	5.6
	KXJ97	2.2	3.2	1.2	2.2
$\Delta\lambda$	HIM91	2.2	–0.36	–0.01	1.4
	KIS98	1.7	–0.30	–0.04	2.5
	KXJ97	1.6	–1.8	–1.0	0.62

mainly comes from the quality of the profile and the estimation of the off-pulse noise level. For KIS98 data, additional error is caused by uncertainty in determining the off-pulse baseline. The errors of relative spectral index shown in Figures 1–3 are obtained with least square fit (Press et al. 1992).

3 RESULTS AND IMPLICATION

The PHRS derived with the data from HIM91, KIS98 and KXJ97 are plotted in the lower panels of Figures 1–3, respectively. The upper panels are the time-aligned multi-frequency profiles adopted from the literature. The dotted vertical lines indicate the profile center at 1.4 GHz that is common to the three data sets. The profile centers at other frequencies are also plotted in the upper panels with open circles. The reference phase bin is marked with arrows. These PHRS results are mutually consistent, in showing generally an "M-like" shape. The major spectral break points divide each PHRS curve into four segments, here labelled as the leading outer (LO), leading inner (LI), trailing inner (TI) and trailing outer (TO) segments, respectively. The boundaries of these segments are shown by dash-dotted lines in the lower panels. The phase interval and total amplitude of fluctuation of the relative spectral index of each segment $\Delta\lambda = \lambda_{\rm inner} - \lambda_{\rm outer}$ are listed in Table 2, where the subscripts "inner" and "outer" denote the inner and outer boundaries of the segments. From the listed values one can see slight differences in the phase intervals of LO and TO between the HIM91 and KIS98 results, and also in their and spectral-index amplitudes. These discrepancies are probably caused by the different observing frequencies used in HIM91 and KIS98. The shorter intervals of the outer segments in the KXJ97 results are mainly due to the narrower profile width at high frequencies. The spectral-index amplitudes of the inner segments are much larger in KXJ97 than those in HIM91 or KIS98, and the "LI" segment is more extended in KXJ97 than in the other two. This may be partially caused by misalignment of profile centers at most frequencies in KXJ97, and partially by possible discontinuous spectral behavior of the bridge emission at low and high frequency ranges. In the following we ignore the slight discrepancies, and focus only on the common features of PHRS.

The basic features of the PHRS are summarized under the following four heads. (1) The PHRS is generally symmetric at the leading and trailing parts of the pulse profile, except it is slightly steeper near the trailing than the leading part. (2) On either side the spectrum consists of an inner and an outer segment, about which the PHRS is completely the opposite. As the pulse longitude varies from the profile center to the outer wing, the spectrum keeps flattening first at the inner segment, but after passing through a break longitude (corresponding to a flattest spectral index), it turns increasingly steep at the outer segment. (3) The break longitudes are located inner to the leading and trailing peaks at the highest frequencies, i.e. 10.5 GHz. The physical meaning of the break longitudes will be discussed in Sections 4 and 5. (4) The local minimum relative spectral index in the inner segments is located near the profile centers. The total amplitude of spectral variation in the inner segments is about 0.3 on average, while the total amplitude reaches nearly 2.0 in the outer segments.

We suggest that it is not necessary to explain the pulse profile shrinkage with frequency by employing narrow-band RFM, rather, we can explain the frequency evolution of the relative intensity of different components with the broad-band spectrum. They can be consistently explained with a broad-band interpretation, i.e. PHRS. Assuming that PHRS is the underlying reason, we explain the major features in the pulse profile evolution of B1133+16 as follows. (1) The profile width shrinkage with frequency is caused by the spectral steepening in the outer segment as the pulse longitude sweeps outwards. Supposing the intensities

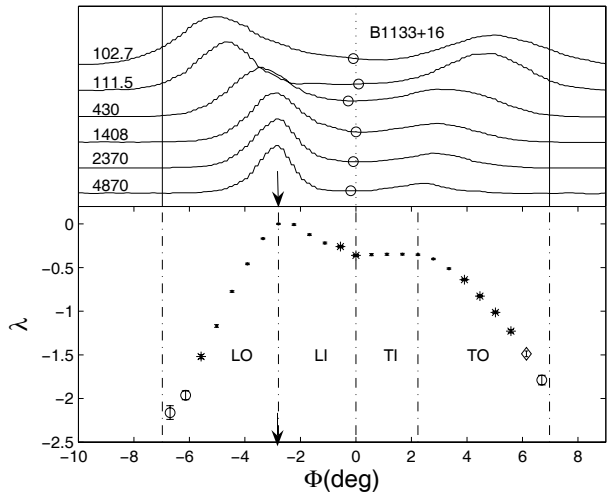

Fig. 1 Phase-resolved spectrum (lower) of B1133+16 derived from the time-aligned profiles (upper) within 102 and 4800 GHz from the HIM91 data. In the upper panel, the frequencies in MHz are marked out for each profile and the open circles mark the profile centers between leading and trailing peaks. In the lower panel, each point is plotted at the corresponding central phase of the re-sampled phase bin. Dotted line: the profile center at 1408 MHz; arrow: the reference phase; solid lines: the longitude boundaries of PHRS; dash-dotted line: the boundaries of each segment. See text for the abbreviation of each segment. The number of relative intensities (or frequencies) used in the fit is represented by the symbol in lower panel: dots - six, stars - five, open diamonds - four, and open circles - three.

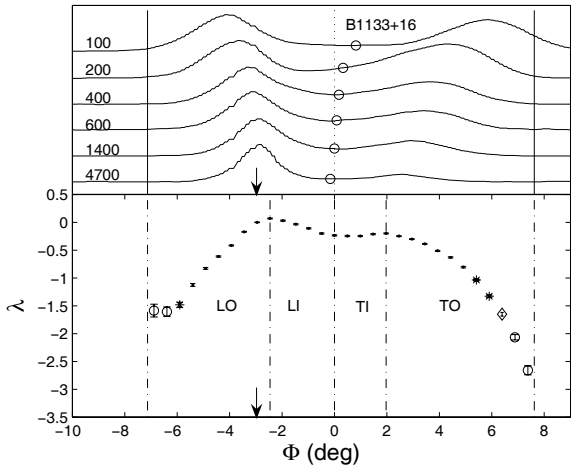

Fig. 2 Phase-resolved spectrum (lower) of B1133+16 derived from the time-aligned profiles (upper) within 0.1 and 4.7 GHz from KIS98. See the caption of Fig. 1 for details.

at two nearby longitudes at the outer segment are initially observable at a low frequency, then, as the frequency increases, the intensity at the outer longitude falls below the noise level, but the inner one may still be above the noise level, because its spectrum is relatively flatter. Thus one will observe the phenomenon of the pulse width decreasing with frequency. (2) Owning to a relatively flatter spectrum near the leading peak, the leading component becomes predominant at high frequency. (3) The bridge emission between the

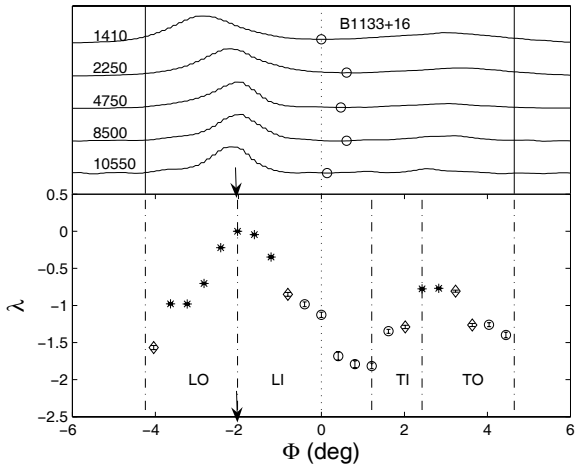

Fig. 3 Phase-resolved spectrum (lower) of B1133+16 derived from the time-aligned profiles (upper) within 1.4 and 10.5 GHz from KXJ97. See the caption of Fig. 1 for details.

two conal components becomes weaker at the high frequency, because its spectrum is the steepest in the inner segment.

4 PHRS: AN INDICATOR FOR SPECTRAL VARIATION ACROSS PULSAR MAGNETOSPHERE?

4.1 Mapping

Since the pulse profile is produced by the line of sight (LOS) sweeping across successive emission regions in the pulsar magnetosphere, it is possible that PHRS reflects the spectral variation across the pulsar magnetosphere, and a detailed mapping will depend on the way a given pulse longitude is related with a specific location of the magnetosphere. In the following only the simplest cases are considered. In order to delineate clearly the connection, three presumptions are made for simplicity. (1) The magnetic field is a pure dipolar field. (2) The emission direction is tangent to the magnetic field line. Retardation, aberration and magnetic field line sweep-back effects are neglected. (3) The emission region is symmetrical about the meridian plane containing the magnetic and rotational axes, hereafter the $\Omega - \mu$ plane, in which Ω and μ representing the rotation and magnetic axes, respectively.

We first consider two extreme cases: case A where the multi-frequency emission originates from the last open field lines, and case B where the emission originates in all the open field lines at a single altitude. The open field lines are distinguished from one another by two parameters, the magnetic azimuth angle φ and the colatitude $\theta_{\rm f}$ of their foot points on the polar cap surface. The azimuth is counted anticlockwise from the $\Omega - \mu$ plane. A third relevant parameter is the emission altitude, denoted by r, and counted from the stellar center. In case A, when the LOS sweeps across the magnetosphere, the emission altitude where the emission direction is aligned with the LOS decreases first in the leading part and then increases in the trailing part. The minimum altitude viewed by the LOS is located at the last open field line on the $\Omega - \mu$ plane. In case B, the magnetic colatitude decreases first and then increases as the LOS sweeps from the leading to the trailing open field lines.

Thus, the PHRS can be translated into a spectral variation with the emission altitude in case A or with the magnetic colatitude in case B. The respective results are plotted in Figures 4 and 5. The emission altitude and colatitude are figured out from pulse longitude with the widely used relations of beam geometry and dipolar field, given in the Appendix. In Figure 4 the abscissa is marked in both absolute and relative altitudes, the latter relative to the maximum derived altitude. The viewing geometry parameters, i.e., the inclination angle $\alpha = 24.9$ and $\beta = 2$ used in the calculation, were adopted from LM88. The altitudes or colatitudes derived from the leading and trailing parts of the profile are marked by dots and diamonds, respectively.

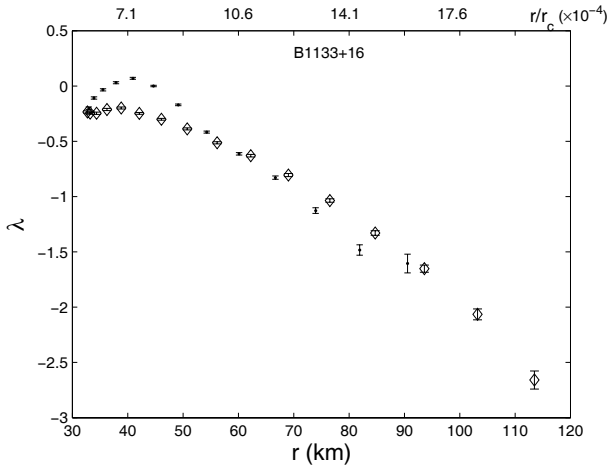

Fig. 4 Relative spectral index versus emission altitude in case A. The leading part and trailing part are marked with dots and diamonds, respectively.

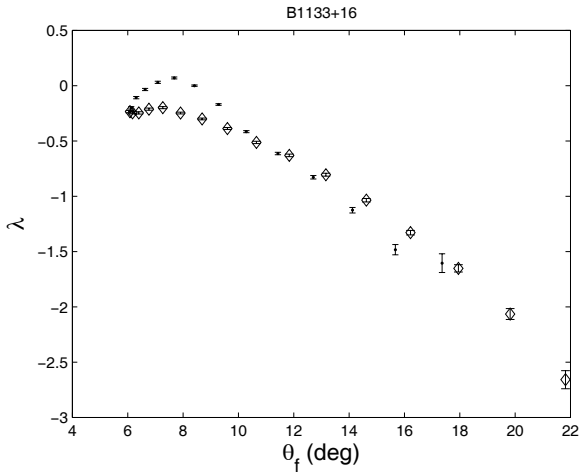

Fig. 5 Relative spectral index versus emission colatitude of foot point of field line in case A. The leading part and trailing part are marked with dots and diamonds, respectively.

In both cases, the two segments in the PHRS reflect spectral variations that are altitude-dependent or colatitude-dependent. In case A the emission spectrum keeps on flattening at first as the emission altitude increases, and then turns to steepening after passing through a critical altitude that corresponds to the break longitude. In case B the emission spectrum keeps on flattening at first as the colatitude increases, i.e. as the open field line shifts outwards with respect to the magnetic axis, and then it turns to steepening after passing through a critical colatitude.

Finally we turn to the third case where the PHRS reflects spectral variation with the magnetic azimuth. Noticing that the successive change of pulse longitude corresponds to successive change of magnetic azimuth, this case may be possible if the emission spectrum does not vary with altitude and colatitude, in which the azimuth is smoothed out for each longitude with Equations (A.1) and (A.2) and plotted in Figure 6, where $\varphi = 0$ denotes $\Omega - \mu$ plane.

To summarize, the PHRS can be an indicator for spectral variation over different locations in the magnetosphere. The emission spectrum may vary with the emission altitude, or magnetic colatitude, or magnetic azimuth in the simplest cases, or with a combination of these factors in complex cases.

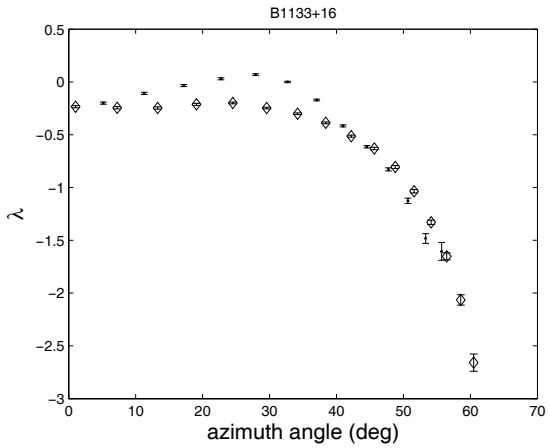

Fig. 6 Relative spectral index versus azimuth of foot point of field line in case A. The leading part and trailing part are marked with dots and diamonds, respectively.

Efforts on the theoretical study of the mechanisms causing spectral variations in the pulsar magnetosphere could clarify which factor is the most important. In the case that the radio emission is from a bunch of charged particles, it has been suggested that the emission spectral index α is related to the particle energy spectral index n by the simple equation $\alpha = (n-1)/2$ or $\alpha = (n-2)/3$ according as the emission mechanism is inverse Compton scattering or curvature radiation (Zhang et al. 2000; Qiao et al. 2001). Then the intrinsic causes of emission spectral variation across the magnetosphere could be attributed to particle spectral variation.

4.2 Candidate Mechanisms for Variation of Particle Energy Spectrum

At least three mechanisms may influence the evolution of particle energy spectrum as secondary particles flow along a magnetic flux tube. The first is resonant inverse Compton scattering (RICS). In the rest frame of a secondary electron, when the Doppler-boosted energy of a soft X-ray photon radiated from the hot stellar surface is equal to the cyclotron energy, the cross section of the electron and photon is essentially enhanced. The electron will lose considerable fraction of its energy due to RICS when it moves from near the stellar surface to altitudes of a few stellar radii. It has been demonstrated that the particle energy spectrum can be changed greatly, generally in opposite directions at lower-energy (steepening) and high-energy (flattening) regimes (see Figs. 5 and 6 in Lyubarskii & Petrova 2000).

The second factor is cooling due to other radiation mechanisms. Synchrotron radiation is possibly an effective one under appropriate values of the pitch angle. Although the synchrotron radiation of secondary particles does not contribute to radio emission in a strong magnetic field, it can affect the particle energy spectrum. Since high energy particles lose energy faster than low energy particles, the particle energy spectrum tends to become steeper as the particles flow outwards.

The third factor is the gamma-B process which may flatten the particle energy spectrum. At a lower height where the magnetic field is still strong enough, e.g. $B > 10^9 - 10^{10}$ G, energetic gamma-ray photons ($h\nu \sim 1 - 10$ GeV) generated by primary relativistic particles ($\gamma \sim 10^6 - 10^7$) can still be converted into electron/positron pairs with $\gamma \sim 10^3 - 10^4$ via the gamma-B process. This effect may compensate for the loss of the number of energetic secondary particles in the bunch, and hence will tend to flatten the particle energy spectrum.

These mechanisms should affect the particle energy spectrum along the altitude, and maybe along the colatitude or azimuth as well. Below we focus on the altitude-dependent effect. The RCIS and gamma-B mechanisms probably take effects within a low altitude range above the polar cap, while the cooling effect may last for a larger distance range. Then the viewing geometry, mainly the impact angle β, is very important for producing the different types of PHRS, because small impact angles usually represent low altitudes viewed by the LOS while large impact angles correspond to large altitudes. In this sense, the break

longitude also has a physical meaning: it indicates the altitude where the dominant mechanisms change over.

Using the correlation $\alpha = (n-1)/2$ or $\alpha = (n-2)/3$, a fluctuation amplitude of emission spectral index of 2 should result from a variation of particle energy spectral index of 5 or 8, or even less if coherent emission mechanisms are also considered. If these mechanisms are proved to be capable of producing large enough amplitudes of spectral index variation, then it is hopeful that the derived PHRS of B1133+16 can be interpreted with specific viewing geometry.

5 CONCLUSIONS AND DISCUSSION

We have derived a PHRS for B1133+16 with the time-aligned multi-frequency profiles published in the literature. It shows an "M-like" shape, and is approximately symmetrical between the leading and trailing parts, except for a slight difference in spectral index between the leading and trailing profile peaks. In each part the spectrum consists of two separated segments. The inner segment gets more flattened and the outer segment steeper as the pulse longitude sweeps from the center to the edge of the pulse profile. The spectrum at the profile center is the steepest in the inner segment. On the assumption that the PHRS is the inherent reason for the frequency evolution of pulse profiles, the major features in the pulse profile evolution of B1133+16, i.e. the pulse width shrinkage at high frequencies, and the frequency development of relative intensity of components can be consistently explained. The PHRS may be an indicator for spectral variation across the pulsar magnetosphere. Possible dependence of the emission spectral index on the emission altitude, or magnetic colatitude, or magnetic azimuth is derived in the simplest cases. Both observational studies on PHRS for a large sample of pulsars and theoretical studies are needed for an understanding of the key factors that cause spectral variation across the magnetosphere.

5.1 Validity of PHRS Results

The assumption of a single power-law spectrum at each phase interval is valid for most intervals, where the values of χ^2 are less than 15, for four to six data points. The corresponding probability of the intervals is larger than 0.001, which means the single power-law fit is acceptable (Press et al. 1992). For those intervals (a few intervals near the trailing peak and a few in the bridge part) where the χ^2 values are larger, the probability is less than 0.001, then a power law could be only regarded as an approximation to the spectrum.

To test the stability of the PHRS results, the reference phase bin was changed among the bins with strong intensities at both the leading trailing parts, and the bin size was changed from about 0.3 ° to 1.2°. In all cases, only slightly differences appeared in the shape and amplitude of the spectral index variation. We also derived a PHRS with only the profiles above 400 MHz in HIM91 and KIS98, the results did not differ much from the PHRS presented in Section 3.

The alignment of multifrequency pulse profiles is different in the three data sets, as can be seen from Figures 1–3. This is because the reduction of DM and the timing models used by the three groups are different. The true relative positions of multifrequency profile centers are not known exactly because of the uncertainty of DM values and other factors in the observations. One can not exclude the possibility that the profile centers are intrinsically aligned at all frequencies. Here, we align the profile centers by hand for KIS98 and KXJ97, in order to find out how the uncertainty in the profile-center alignment affects the validity of the derived PHRS. The obtained PHRS are shown in Figures 7 and 8. The profile-center realigning is not performed for HIM91, because the centers therein are nearly aligned. With the centers re-aligned, the PHRS curve of KIS98 is nearly the same as that of HIM91. The amplitude of PHRS variation in KXJ is decreased. Although the shape of the "LI" segment is a little different from the previous result, the general shape now resembles more that of the PHRS of HIM91 and KIS98. Comparing with the earlier and later PHRS results, one finds that the shape of PHRS did not change much by the realigning of the profile centers.

With the above tests, we have verified that the general properties of the PHRS presented here are valid.

5.2 Alternative Interpretations for Observational Features of B1133+16

Although the PHRS can be used to explain coherently the basic observational features in the profile evolution of B1133+16, and it is suggested that some physical mechanisms may be intrinsic for PHRS, other possible interpretations for the observed features can not be excluded.

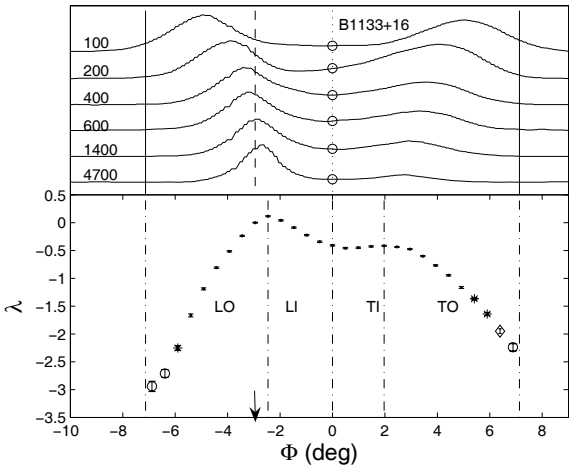

Fig. 7 Phase-resolved spectrum (lower) derived for KIS98 after the profile centers are realigned (upper).

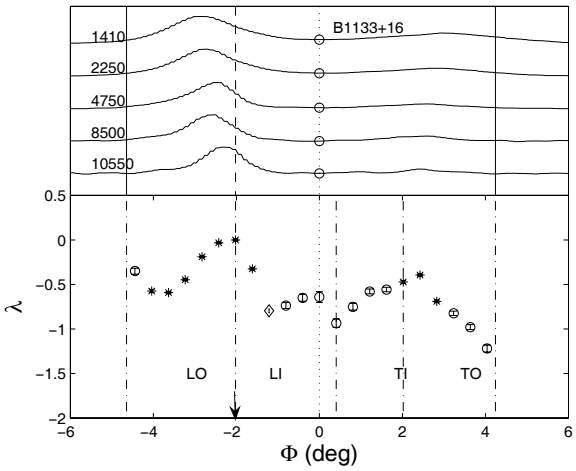

Fig. 8 Phase-resolved spectrum (lower) derived for KXJ97 after the profile centers are realigned.

As a broad-band emission model, Barnard & Arons (1986) presented the refraction effect on the frequency dependency of the pulse width. In one of the scenarios considered in the paper, it is assumed that multifrequency emission is radiated from a single altitude. By involving the refraction effect when radio waves propagate through a magnetospheric plasma with a constant density distribution or a steep transverse plasma density gradient towards the magnetic pole, the model can explain the phenomena of pulse width shrinkage or near constancy with frequency. In this model, because low-frequency radio waves are bent by a larger angle than high-frequency waves due to refraction, the pulse profile becomes broader at a lower frequency. If this scenario is true for B1133+16, then NRRS would not be a more meaningful way than PHRS for representing the spectral variation across the emission beam or different locations of the magnetospheric.

In the inverse Compton scattering (ICS) model (Qiao 1988; Qiao & Lin 1998; Qiao et al. 2001; Qiao et al. 2002), the radio emission is generated via ICS between the secondary relativistic particles and the low-frequency waves that are produced via oscillatory sparking in the inner vacuum gap. Various profile types and changes with frequency can be reproduced by a simple relation between the frequencies of scattered

and injection waves, $\nu \simeq \gamma^2 \nu_0 (1-\beta\cos\theta_i)$, where $\gamma = 1/(1-\beta)^{1/2}$ is the Lorentz factor of particle, θ_i the incident angle between the directions of particle and injection photon at an emission point. Assuming that the Lorentz factor decreases significantly as the particles move in the magnetic field, this relation predicts a three-segment frequency-altitude relation (fig. 6 in Qiao & Lin 1998): as the emission altitude r increases, the emission frequency first sharply decreases to near zero, then increases, and then decreases again. Thus the emission at a single frequency can be generated at three altitudes, producing the core, inner conal and outer conal beams. Because the opening angle is proportional to $r^{1/2}$, the frequency dependency of the core or conal beam angular size is similar to the altitude-frequency relation at the corresponding segment, i.e. the core and outer conal beam sizes decrease with frequency, while the inner conal beam size increases with frequency.

The above relations are based on the assumption that the secondary particles have a single value of Lorentz factor at any location. This is essentially a narrow-band scenario, i.e., at a given altitude radiation around a single frequency is emitted. Noticing that emission has been observed over wide frequency range for most pulse longitudes, it is necessary to extend this model to a broad-band version by considering, e.g., a distribution of Lorentz factors in a bunch of particles, but in any way, those relations should be still valid in this extended broad-band version. In this case, we may hopefully explain the profile shrinkage of B1133+16 with the ICS model in a simple manner, i.e., the frequency behavior of the outer conal emission segment. Then, the PHRS is no longer an intrinsic factor, but only a by-product of the frequency behavior of the conal component due to the ICS emission.

5.3 Comparison with the Results of PHRS and NRRS

For comparison, the phase-dependent spectra derived from HIM91 data with NRRS are presented in Figure 9. In the upper panel the profile is normalized to unity at both the leading and trailing halves at each frequency. The pulse profile boundaries are determined by the 10% level of the corresponding peaks, i.e., the leading (trailing) boundary to the leading (trailing) peak. The normalized phase is divided into nine bins for both halves; the relative spectral index is calculated with respect to the trailing outmost bin. Unlike LM88, the pulse longitude is not translated into beam radius. Keeping in mind that inner phase bin corresponds to inner beam radius, the derived normalized-phase-resolved spectra (NPHRS) can represent the NRRS, therefore in the following we do not distinguish between NPHRS and NRRS. A noticeable feature in NRRS is that the spectra in the trailing half are generally steeper than those in the leading half. The feature of the spectrum steepening with increasing amplitude at the outer segment in PHRS does not appear in NRRS. This absence is a direct consequence of the normalization of the pulse longitudes. If the multifrequency emission does originate from a narrow altitude range and undergoes refraction, as is suggested by the wave propagation model (Barnard & Arons 1986), the derived NRRS would be a better representation for the emission spectral variation in different emission locations.

5.4 Large Sample Study of PHRS

A PHRS study for a large sample of pulsars may reveal more information on the connection between PHRS and profile evolution with frequency. At least, one may explore this issue on two aspects.

First, similar to B1133+16, a number of pulsars published in the literature (Hankins & Rickett 1986; KIS98; KXJ97) showed pulse width shrinkage with frequency, e.g. B0525+21, B1237+25. Therefore, their PHRS are expected to have the same feature as the outer segments of B1133+16. However, some pulsars exhibit the opposite frequency behavior, e.g. B1604–02, where two outer segments get stronger with increasing frequency. Multifrequency studies on the pulse width evolution for a number of pulsars have confirmed that for most pulsars, the pulse width shrinks or stays nearly constant with increasing frequency, while for a small fraction of pulsars the pulse width increases with frequency (e.g. Kijak et al. 1998). Therefore, it is interesting to explore how different types of PHRS are responsible for different kinds of profile width behavior.

The second aspect is the association between the PHRS and the core and conal components. The core-conal classification is an empirical description for components with different observational properties, e.g. spectral behavior, polarization (Rankin 1983). PSR B1133+16 is a classical double-conal pulsar, of which the outer conal components dominate the profile (Rankin 1990; Mitra & Rankin 2002). In this paper, B1133+16 shows nearly asymmetric PHRS behavior in the leading and trailing conal components. It

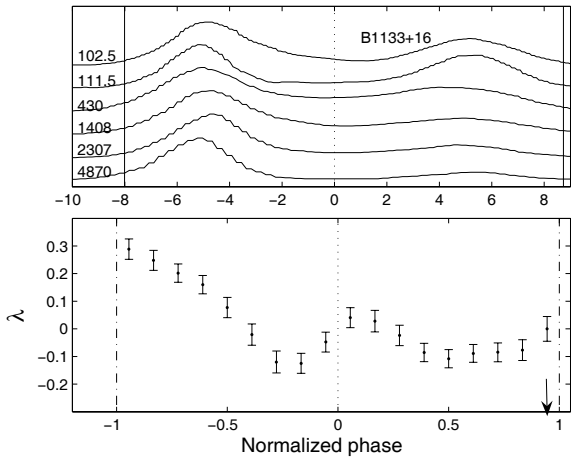

Fig. 9 Phase-dependent spectra obtained with the NRRS method. The time-aligned profile, adopted from HIM91, is normalized to unity in both the leading and trailing parts of the profile at each frequency.

is worth testing if B1133+16-like PHRS is common for the outer conal components, or, on the other hand, if the core and conal components have different types of PHRS behavior.

Acknowledgements We are grateful to the members of pulsar group at Peking University, A. Jessner, J. L. Han, R.N. Manchester and the colleagues of CfA at Guangzhou University for their valuable discussions and comments. We appreciate the anonymous referee for his/her valuable suggestion. This work was supported by the National Natural Science Foundation of China (NSFC, Grants 10373002 and 10403001).

Appendix A: THE GEOMETRICAL RELATIONS

We present here the equations that the observing pulse longitude Φ relates to the emission altitude r, field-line-foot-point colatitude $\theta_{\rm f}$ and azimuth φ. These parameters are defined in a spherical coordinate in which the polar axis is magnetic axis and the origin is the pulsar center.

Under the three assumptions made in Section 4, the pulse profile center corresponds to the emission from $\Omega - \mu$ plane, i.e., $\Phi = 0$ corresponds to $\varphi = 0$.

Given an inclination angle α between the rotation and magnetic axes and a viewing angle ζ between line of sight and rotation axis, the azimuth can be figured out with

$$\cos\varphi = \frac{\cos\alpha\cos\theta_\mu - \cos\zeta}{\sin\alpha\sin\theta_\mu}, \tag{A.1}$$

where θ_μ is the opening angle between emission direction and magnetic axis, which reads (Zhang et al. 2007)

$$\cos\theta_\mu = \cos\alpha\cos\zeta + \sin\alpha\sin\zeta\cos\Phi. \tag{A.2}$$

Under a dipolar magnetic field geometry, the polar angle θ of the emission point at a specific open field line can be solved from an opening angle by

$$\tan\theta_\mu = \frac{3\sin 2\theta}{1 + 3\cos 2\theta}. \tag{A.3}$$

When one specifies a magnetic field line, i.e. the colatitude of the foot point of this field line $\theta_{\rm f}$ is fixed, just like case A in Section 4, the emission altitude follows

$$r = R_{\rm e}(\theta_{\rm f,lof}/\theta_{\rm f})^2\sin^2\theta, \tag{A.4}$$

where $\theta_{\rm f,lof}$ is the colatitude of the foot point of last open field line, and $R_{\rm e}$ is the maximum radius of the last open field line. They are both functions of α and φ, but as a good approximation they can be replaced by the light cylinder radius $R_{\rm c} = Pc/2\pi$ and $\theta_{\rm f,lof} \simeq (R/R_{\rm c})^{1/2}$, where P is pulsar period, R the stellar radius, usually $R = 10\,$km is assumed.

Alternatively, if one fixes the emission altitude, like the case B mentioned in Section 4, the colatitude $\theta_{\rm f}$ can be derived from Equation (A.4).

References

Barnard J. J., Arons J., 1986, ApJ, 302, 138
Cordes J. M., 1978, ApJ, 222, 1006
Fierro J. M., Michelson P. F., Nolan P. L., Thompson D. J., 1998, ApJ, 494, 734
Hankins T. H., Rickett B. J., 1986, ApJ, 311, 684
Hankins T. H., Izvekova V. A., Malofeev V. M. et al., 1991, ApJ, 373, 17 (HIM91)
Jackson M. S., Halpern J. P., 2005, ApJ, 633, 1114
Kanbach G., Arzoumanian Z., Bertsch D. L. et al., 1994, A&A, 289, 855
Kijak J., Kramer, M., Wielebinski R., Jessner A., A&AS, 127, 153
Kramer M., Karastergiou A., Gupta Y. et al., 2003, A&A, 407, 655
Kramer M., Wielebinski R., Jessner A. et al., 1994, A&A, 107, 515 (KWJ94)
Kramer M., Xilouris K. M., Jessner A. et al., 1997, A&A, 322, 846 (KXJ97)
Kuiper L., Hermsen W., Cusumano G. et al., 2001, A&A, 378, 918
Kuzmin A. D., Izvekova V. A., Shitov Yu. P. et al., 1998, A&AS, 127, 355 (KIS98)
Lyubarskii Y. E., Petrova S. A., 2000, A&A, 355, 406
Lyne A. G., Manchester R. N., 1988, MNRAS, 234, 477 (LM88)
Maron O., Kijak J., Kramer M., Wielebinski R., 2000, A&AS, 147, 195
Mineo T., Ferrigno C., Foschini L. et al., 2006, A&A, 450, 617
Mitra D., Rankin J. M., 2002, ApJ, 577, 322
Phillips J. A., 1991, ApJ, 373, L63
Popov M. V., Soglasnov V. A., 1987, Sov. Astron. Lett., 13, 11
Press W. H., Teukolsky S. A., Vetterling W. T., Flannery B. P., 1992, Numerical Recipes, second edition, Cambridge: Cambridge University Press, p.651
Rankin J. M., 1983, ApJ, 274, 359
Rankin J. M.,1990, ApJ, 352, 247
Qiao G. J., 1988a, Vistas in Astronomy, 31, 393
Qiao G. J., Lin W. P., 1998, A&A, 333, 172
Qiao G. J., Liu J. F., Zhang B., Han J. L., 2001, A&A, 377, 964
Qiao G. J., Wang X. D., Wang H. G. et al., 2002, Chin. J. Astron. Astrophys. (ChJAA), 2, 361
Taylor J. H., Manchester R. N., Lyne A. G., 1993, ApJS, 88, 529
Thorsett S. E., 1991, ApJ, 377, 263,
Wang H. G., Han J. L., Qiao G. J., 2001, Chin. Astron. Astrophy., 25, 73
Wang H. X., Wu X. J., 2003, Chin. J. Astron. Astrophys. (ChJAA), 3, 469
Wang N., Wu X. J., Manchester R. N., 2001, Chin. J. Astron. Astrophys. (ChJAA), 1, 421
Wu X. J., Xu W., Rankin J. M., 1992, In: T. H. Hankins, J. M. Rankin, J. A. Gil, eds., IAU Collq. 128, The Magnetospheric Structure and Emission Mechanism of Radio Pulsars., Zielona Gora Poland: IAU, p.172
Wu X. J., Huang Z. K., Xu X. B., 2002, Chin. J. Astron. Astrophys. (ChJAA), 2, 454
Zhang H., Qiao G. J., Lee K. J. et al., 2007, A&A, 465, 525
Zhang J. L., Xia T. S., Yang J. M., 2000, Physics Letter A, 275, 315